

# An eigenerosion approach to brittle fracture

A. Pandolfi<sup>1,\*†</sup> and M. Ortiz<sup>2</sup>

<sup>1</sup>Dipartimento di Ingegneria Strutturale, Politecnico di Milano, Piazza Leonardo da Vinci 32, 20133 Milano, Italy  
<sup>2</sup>Graduate Aeronautical Laboratories, California Institute of Technology, Pasadena, CA 91125, USA

## SUMMARY

The present work is concerned with the verification and validation of a variant of the eigenfracture scheme of Schmidt *et al.* (2009) based on element erosion, which we refer to as *eigenerosion*. Eigenerosion is derived from the general eigenfracture scheme by restricting the eigendeformations in a binary sense: they can be either zero, in which case the local behavior is elastic, or they can be equal to the local displacement gradient, in which case the corresponding material neighborhood is failed or *eroded*. When combined with a finite-element approximation, this scheme gives rise to *element erosion*, i.e., the elements can be either intact, in which case their behavior is elastic, or be completely failed, or eroded, and have no load bearing capacity. We verify the eigenerosion scheme through comparisons with analytical solutions and through convergence studies for mode I fracture propagation, both in two and three dimensions and for structured and random meshes. Finally, by way of validation, we apply the eigenerosion scheme to the simulation of mixed modes I–III experiments in poly-methyl methacrylate plates. <sup>‡</sup> Copyright © 2012 John Wiley & Sons, Ltd.

Received 24 December 2011; Revised 10 April 2012; Accepted 13 April 2012

KEY WORDS: finite elements; eigenerosion; Griffith's theory of fracture; mixed mode fracture; convergence analysis

## 1. INTRODUCTION

Recently, [1] have proposed an approximation scheme for variational models of Griffith's theory of fracture (cf., e.g., [2–10]). Within this variational framework, fracture is viewed as a *free-discontinuity problem*, i.e., a problem where the solution can have discontinuity points [11] and, in addition, the jump sets of the solution are *a priori* unknown [4, 10, 12, 13]. The scheme, which Schmidt *et al.* termed *eigenfracture*, is based on the notion of *eigendeformation*. Eigendeformations are widely used in mechanics to describe deformation modes that cost no local energy [14]. In the eigenfracture scheme, the energy functional depends on two fields: the displacement field  $u$  and an eigendeformation field  $\varepsilon^*$  that describes such cracks as may be present in the body. Specifically, eigendeformations allow the displacement field to develop jumps at no cost in local elastic energy. In addition, in the eigenfracture scheme, the fracture energy is set to be proportional to the volume of the  $\epsilon$ -neighborhood of the support of the eigendeformation field, suitably scaled by  $1/\epsilon$ . The optimal crack set is obtained by minimizing the resulting energy functional with respect to both the displacement and the eigendeformation fields, subject to irreversibility constraints.

The present work is concerned with the verification and validation of a variant of the eigenfracture scheme, based on element erosion, which we refer to as *eigenerosion*. Eigenerosion is derived from the general eigenfracture formulation by restricting the eigendeformations in a binary sense: they can be either zero, in which case the local behavior is elastic, or they can be equal to the local

<sup>\*</sup>Dedicated to the memory of Professor Osvaldo De Donato.

<sup>\*</sup>Correspondence to: Anna Pandolfi, Dipartimento di Ingegneria Strutturale, Politecnico di Milano, Piazza Leonardo da Vinci 32, 20133 Milano, Italy.

<sup>†</sup>E-mail: pandolfi@stru.polimi.it

displacement gradient, in which case the corresponding material neighborhood is failed, or *eroded*. When combined with a finite-element approximation, this scheme gives rise to *element erosion*, i.e., the elements can be either intact, in which case their behavior is elastic, or be completely failed, or eroded, and have no load bearing capacity. The implementation of the method, included the all-important  $\epsilon$ -neighborhood construction, is exceedingly simple and applies to general situations, possibly involving complex three-dimensional fracture patterns such as branching and fragmentation. The accuracy and convergence of the eigenerosion approach are comparable—at a much reduced implementation cost and complexity—to that of other numerical fracture schemes.

We note that element erosion has been extensively used to simulate fracture in a number of areas of application, including terminal ballistics [15–20]. However, some of these methods fail to converge or converge to the wrong limit [21]. By contrast, the eigenfracture scheme is known to properly converge to Griffith fracture in the limit of vanishingly small mesh sizes [1]. In particular, the local-neighborhood averaging of the energy that underlies the calculation of the effective energy release has the effect of eliminating spurious mesh dependencies.

The paper is organized as follows. We begin by summarizing parts of the underlying Griffith's theory of fracture that are relevant to this work in Section 2. We describe the numerical implementation in Section 3. Then, we proceed to verify the approach through comparisons with analytical solutions available for linear elasticity in Section 4.1. We present further verification of the approach through convergence studies for mode I crack growth, both in two and three dimensions, in Section 4.2. We conclude with a final three-dimensional example aimed at validating the approach in applications concerned with mixed mode I–III experiments in polymethyl methacrylate (PMMA) plates in Section 4.3.

## 2. VARIATIONAL FORMULATION OF BRITTLE FRACTURE MECHANICS

Throughout this work, we are concerned with the problem of tracking the growth of cracks in perfectly brittle but otherwise linear-elastic materials. To facilitate numerical approximations of the problem, we adopt a variational formulation of fracture mechanics. To this end, we regard fracture as irreversible, dissipative, and driven by energetic driving forces, with all the dissipation attendant to crack growth concentrated on the crack front, and proceed to formulate the *rate problem*, i.e., the problem that determines the rate of advance of the crack. We specifically consider perfectly brittle solids in which the fracture energy is proportional to the area of cracks. The corresponding rate problem embodies Griffith's criterion for crack growth and arrest. Given the rate independence of Griffith's criterion, the crack-tracking problem, i.e., the determination of crack trajectories, can be recast in terms of a deformation-theoretical *energy-dissipation* pseudo-energy that combines the elastic energy of the body and the energy expended in creating new surfaces, subject to conditions of monotonicity of the crack set. This reformulation of the crack-tracking problem can also be expressed in terms of *eigendeformations*, representing the opening displacements of the crack. A regularization of this eigendeformation formulation of the crack-tracking problem proposed by Schmidt *et al.* [1], or *eigenfracture* formulation, is finally taken as a basis for numerical approximation, leading to the element eigenerosion schemes that are the focus of the present work. In this section, we begin by briefly recounting the elements of formal fracture mechanics that underlie the crack-tracking problem of interest and its eigenfracture formulation. We proceed formally and assume regularity and smoothness as required. Mathematically rigorous accounts of the theory may be found, e.g., in [7–9].

We consider an elastic body occupying a three-dimensional domain  $\Omega$ , see Figure 1. The boundary  $\partial\Omega$  of the body consists of an exterior boundary  $\Gamma$ , corresponding to the boundary of the uncracked body, and a collection of cracks jointly defining a crack set  $C$ . In addition,  $\Gamma$  partitions in the usual manner into a displacement boundary  $\Gamma_1$  and a traction boundary  $\Gamma_2$ . The body undergoes deformations under the action of body forces, displacements prescribed over  $\Gamma_1$ , and tractions applied over  $\Gamma_2$ . Under these conditions, the potential energy of the body is

$$E(u, C, t) = \int_{\Omega \setminus C} W(\varepsilon(u)) \, dV - \int_{\Gamma_2} \bar{T} \cdot u \, dS, \quad (1)$$

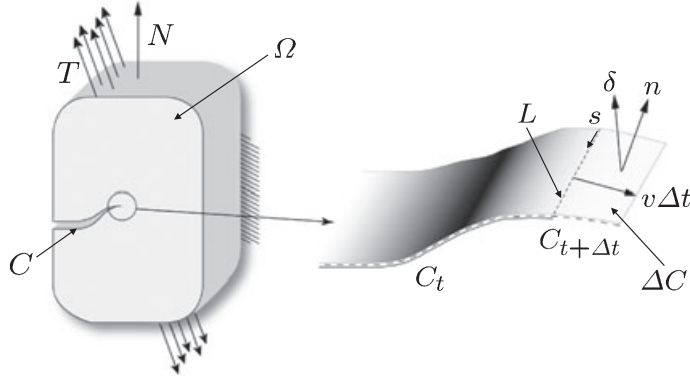


Figure 1. Crack advancing in a body occupying domain  $\Omega$  and zoom of the crack-front region showing the crack set  $C_t$  at time  $t$ , contained with crack set  $C_{t+\Delta t}$  at time  $t + \Delta t$ , during which interval of time, the crack-front  $L$  sweeps an area  $\Delta C$  of unit normal  $n$ . Detail of advancing front  $L$  and definition of front velocity  $v$ .

where  $\Omega \setminus C$  denotes the domain of the body with the crack set excluded,  $dV$  and  $dS$  are the elements of volume and area, respectively,  $W$  is the elastic strain energy density of the body,  $\bar{T}$  is the applied traction, and

$$\varepsilon(u) = \frac{1}{2} (\nabla u + (\nabla u)^T) \quad (2)$$

is the strain operator of linear elasticity. In addition, we must have

$$u(x) = \bar{u}(x), \quad x \in \Gamma_1, \quad (3)$$

where  $\bar{u}$  are the prescribed displacements. The explicit dependence of  $E$  on  $t$  in (1) is meant to reflect the time dependence of the forcing, namely, the applied forces and prescribed displacements. For every crack set  $C$  and time  $t$ , the corresponding equilibrium displacement field follows by minimization of energy (1) over some appropriate space of functions.

Suppose now that the applied loads and prescribed displacements are incremented over the time interval  $[t, t + \Delta t]$  and that, in response to this incremental loading, the crack set extends from  $C(t)$  to  $C(t + \Delta t)$ . By assuming continuing equilibrium throughout crack growth, a standard calculation [22, 23] gives the elastic energy released during the time increment as

$$-\Delta E \sim \int_{\Delta C} T(t) \cdot [\![u(t + \Delta t)]\!] dS, \quad (4)$$

where the symbol  $\sim$  is used to denote quantities of the same order,  $[\![u]\!]$  represents the displacement jump across the crack surface, and we write the extension of the crack set as  $\Delta C = C(t + \Delta t) \setminus C(t)$ , Figure 1. In Equation (4), we denote

$$T(t) = \partial_\varepsilon W(\varepsilon(u)) n \equiv \sigma(\varepsilon(u)) n, \quad (5)$$

where  $n$  is the unit outward normal to the boundary. The symbol  $\partial_\varepsilon$  denotes partial differentiation with respect to  $\varepsilon$ . The corresponding energy-release rate now follows as

$$-\dot{E} = -\lim_{\Delta t \rightarrow 0} \frac{\Delta E}{\Delta t} = \int_L G(n) v \, ds, \quad (6)$$

where  $L$  is the crack front,  $v$  is the crack-front velocity, Figure 1, and

$$G(n) = \lim_{\Delta t \rightarrow 0} T \cdot [\![u(t + \Delta t)]\!] \quad (7)$$

is the energetic force acting on the crack front, or *energy-release rate*, which depends on the direction of crack advance.

Identity (6) expresses the rate at which energy flows to—and is subsequently dissipated at—the crack front. In particular, the duality-pairing structure of (6) is conventionally taken to mean that the energetic force  $G$  does power, or *drives* on the crack-front velocity  $v$ . On this basis, it is customary in irreversible continuum mechanics to postulate the existence of a kinetic relation, or *crack-tip equation of motion*, of the form

$$G = \partial\psi(v), \quad (8)$$

where  $\psi$  is a dissipation potential density per unit crack-front length and  $\partial$  denotes partial differentiation. An application of Coleman and Noll's method [24] additionally gives the dissipation inequality

$$G v \geq 0, \quad (9)$$

which follows as a consequence of the second law of thermodynamics. Dissipation inequality (9) introduces a unilateral constraint that prevents crack healing. This absence of healing in turn introduces the monotonicity constraint

$$C(t) \subset C(t + \Delta t), \quad (10)$$

i.e., later crack sets must contain earlier crack sets. It should be also noted that crack opening is subject to the unilateral contact constraint

$$[u] \cdot n \geq 0. \quad (11)$$

In particular, part or all of the crack set can be closed at any given time.

In view of identity (6), the rate problem of fracture mechanics reduces to

$$\inf_{v,n} \int_F (\psi(v) - G(n)v) ds \quad (12)$$

and the corresponding Euler–Lagrange equations are

$$\partial\psi(v) = G(n), \quad (13a)$$

$$\partial\psi^*(G(n)) = 0, \quad (13b)$$

where  $\psi^*$  is the dual dissipation potential per unit crack-front length, which jointly determines the crack-tip velocity  $v$  and direction of advance  $n$ . The resulting geometry and kinetics of crack advance are illustrated in Figure 2 with the local crack geometry parameterized by arc-length  $s$  and described by orthonormal axes tangent to the crack and its front. Because of constraint (10), it follows that the direction of crack advance can locally be described by means of a single *kinking angle*  $\omega(s)$ , and (13) reduces to one single equation for the determination of  $\omega(s)$ . We note from (12) that the resulting kinking angle maximizes the energy-release rate or, equivalently, the rate of dissipation  $G(n)v$ , and thus, we can regard (12) variously as a maximum energy release or a maximum

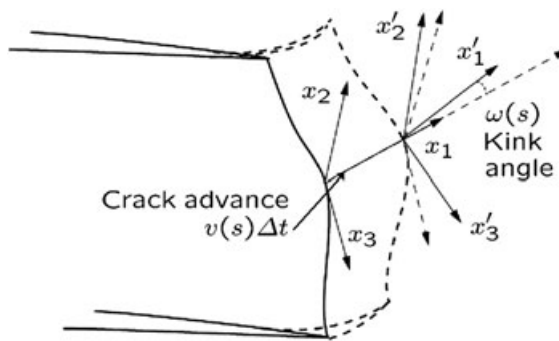


Figure 2. Local view of the geometry and kinetics of crack advance.

dissipation principle. Once  $\omega(s)$ , and by extension  $n(s)$ , is determined from (13), the local crack-front velocity  $v(s)$ , giving the rate of extension of the crack, follows from the crack-tip equation of motion (13a).

For a perfectly brittle material, the dissipation potential takes the *rate-independent* form

$$\psi(v) = G_c |v|, \quad (14)$$

where  $G_c$  is the critical energy-release rate, or specific fracture energy, of the material and  $|v|$  is the norm of the velocity  $v$ . Because  $\psi(v)$  is not differentiable at the origin, the equation of motion (8) must be understood in the sense of subdifferentials, namely,

$$G - G_c \leq 0, \quad (15a)$$

$$v \geq 0, \quad (15b)$$

$$(G - G_c)v = 0, \quad (15c)$$

which embody Griffith's crack propagation and arrest criteria. Because of the rate-independent nature of Griffith's criterion, the crack-tracking problem can be reduced to the minimization of the energy-dissipation functional

$$F(u, C, t) = E(u, C, t) + G_c |C| \quad (16)$$

at every time, subject to monotonicity constraint (10). In (16),  $|C|$  denotes the area of the crack set. Thus, the geometry of a growing crack and the corresponding equilibrium elastic field in a perfectly brittle material is obtained by minimizing  $F(u, C, t)$  at all times with respect to both the displacement field  $u$  and the crack set  $C$  subject to constraint (10). Conditions for the existence of solutions of this coupled problem, which is not guaranteed in general, may be found in [7–9]. As may be seen from (16), the crack path results from a competition between the following: the elastic energy, which promotes fracture as an energy-release mechanism; the specific fracture energy, which penalizes fracture proportionally to the crack area; and the monotonicity and contact constraints, (10) and (11), respectively, which introduce irreversibility, path dependency, hysteresis, and tension-compression asymmetry.

To obviate the need for minimizing the energy-dissipation functional  $F(u, C, t)$  with respect to the crack set  $C$ , which may be numerically cumbersome, we proceed to reformulate the crack-tracking problem in terms of *eigendeformations*. We begin by introducing the extended elastic energy

$$E(u, \varepsilon^*, t) = \int_{\Omega} W(\varepsilon(u) - \varepsilon^*) dV - \int_{\Gamma_2} \bar{T} \cdot u dS, \quad (17)$$

where the eigendeformations  $\varepsilon^*$  are restricted to be of the form

$$\varepsilon_{ij}^* = \frac{1}{2}(\delta_i n_j + \delta_j n_i) \delta_C. \quad (18)$$

Here,  $\delta = [\![u]\!]$  represents the opening displacement field across  $C$ ,  $n$  represents the unit normal to  $C$ , and  $\delta_C$  represents a distribution concentrated over the crack set  $C$ , i.e., a distribution such that

$$\delta_C(\varphi) = \int_C \varphi dS \quad (19)$$

for all test functions  $\varphi$ . We note that, by virtue of the preceding extension, the crack set and the attendant opening displacements, which are now regarded as independent variables, are accounted for jointly by the eigendeformation field  $\varepsilon^*$ . The introduction of eigendeformations allows the displacement field to develop jumps that cost no local elastic energy. In addition, energy minimization with respect to the opening displacement field  $\delta$  results in displacements that satisfy zero-traction boundary conditions over the crack set, and we have

$$E(u, C, t) = \inf_{\delta} E(u, \varepsilon^*, t), \quad (20)$$

where the minimization is to be effected over some appropriate space of traces. Thus, the new reformulation of the problem is equivalent to the original one.

The extended energy  $E(u, \varepsilon^*, t)$  can now be taken as a basis for formulating variational *element erosion* approximation schemes. For instance, a typical scheme consists of introducing  $C^0$  finite-element interpolation for the displacements and piecewise constant interpolation for the eigen-deformations, i.e., restricting the eigendeformations to be constant over the elements, although not necessarily rank-one symmetric as in (18) [17]. These schemes indeed converge pointwise as the mesh size goes to zero, provided that the crack set is aligned with the mesh, but may fail to converge otherwise [21]. The reason for the lack of convergence is a geometrical one: as the crack zigzags in accordance with the mesh to match the limiting crack path, it overestimates the amount of fracture energy by a geometrical factor. Negri developed converging schemes that overcome this difficulty by recourse to mesh adaption [21, 25] or to nonlocal averaging schemes [26, 27].

In this work, we follow Schmidt *et al.* [1] who formulated convergent element erosion, or *eigen-erosion*, schemes by means of a regularization of extended energy (17). The net effect of this regularization is to eliminate the spurious mesh-dependencies that afflict naive erosion schemes and ensure convergence of the approximations. The regularized energy-dissipation functional proposed by Schmidt *et al.* [1] is

$$F_\epsilon(u, \varepsilon^*, t) = \int_{\Omega} W(\varepsilon(u) - \varepsilon^*) \, dV - \int_{\Gamma_2} \bar{T} \cdot u \, dS + G_c \frac{|C_\epsilon|}{2\epsilon}. \quad (21)$$

In these expressions,  $\epsilon$  is a small parameter with units of length;  $C = \{\varepsilon^* \neq 0\}$  is the support of the eigendeformation field, i.e., the domain over which the eigendeformation field is nonzero, which may be regarded as an approximation to the crack set;  $C_\epsilon$  is the  $\epsilon$ -neighborhood of  $C$ , i.e., the set of points that are at a distance less or equal to  $\epsilon$  from  $C$ ; and  $|C_\epsilon|$  denotes the volume of the  $\epsilon$ -neighborhood  $C_\epsilon$ . We note that the regularized energy-dissipation functional  $F_\epsilon(u, \varepsilon^*, t)$  now allows for eigendeformation fields that are spread over a volume and thus represent a damaged volume of material. As before, the eigendeformations allow the material to relax its energy locally. The crux of the approach of Schmidt *et al.* [1] concerns the proper evaluation of the fracture-energy cost attendant to a distribution of eigendeformations, which is given by the last term in (21). Indeed, Schmidt *et al.* [1] have shown that the regularized energy-dissipation functional  $F_\epsilon$ , Equation (21),  $\Gamma$ -converges to the Griffith functional  $F$ , Equation (16), as  $\epsilon \rightarrow 0$ . We recall that  $\Gamma$ -convergence is a notion of variational convergence that implies convergence of minimizers. In particular, the scaling of the volume of the  $\epsilon$ -neighborhood  $C_\epsilon$  by  $\epsilon^{-1}$  in energy-dissipation functional (21) in turn penalizes the volume of the approximate crack set  $C$ , which in the limit converges to a surface.

The regularized crack-tracking problem consists of minimizing the regularized energy-dissipation functional (21) for every time subject to monotonicity constraint (10), which now requires that the approximate crack sets grow monotonically, and to a suitable contact constraint in lieu of (11). For instance, the constraint

$$\varepsilon^* \geq 0, \quad (22)$$

first proposed by Ortiz [28] and widely used since, can be used to enforce the contact constraint within an eigendeformation framework. Constraint (22) specifically requires that all the eigenvalues of  $\varepsilon^*$  be nonnegative, which effectively satisfy the crack closure constraint.

The remainder of this paper is devoted to a verification and validation analysis of finite-element approximation schemes based on the regularized crack-tracking problem just described. We note that other two-field approximation schemes for brittle fracture, most notably the Ambrosio-Tortorelli scheme [2, 4], have been proposed in the past and used as a basis for numerical approximations [29–31], but the use of eigendeformations to describe brittle fracture in a variational framework does not appear to have been pursued prior to Schmidt *et al.* [1]. We also note that other damage regularizations of brittle fracture [3, 4, 10, 26] have been proposed in the past and shown to be convergent.

### 3. NUMERICAL IMPLEMENTATION

Schmidt *et al.* [1] have further proved that finite-element approximations of the regularized problem converge to exact solutions of the Griffith crack-tracking problem when the mesh size and the regularization parameter tend to zero in the right order. One specific scheme that was shown to be convergent consists of approximating the displacement field by means of conventional  $C^0$  finite-element interpolation and taking the eigendeformation field to be constant over elements but otherwise unconstrained. Because the local element eigendeformations are allowed to take arbitrary values, they are either zero to minimize the attendant fracture energy or completely negate the local deformation of the element, thus rendering its elastic energy zero. Thus, in this approximation scheme, the discrete crack-tracking problem is reduced to successively *failing* or *eroding* elements when the attendant elastic energy release exceeds the attendant cost in fracture energy. The energy-release rate attendant to the erosion of one element can be computed explicitly, as the difference of the energies of the body before and after the erosion of the element, or more conveniently, it can be approximated using first-order asymptotic formulae for notches [17]. The fracture-energy cost is computed by recourse to the  $\epsilon$ -neighborhood construction, as further discussed in the following text.

---

**Algorithm 1** Crack-tracking scheme

---

**Require:** Crack set  $C_n$  at time  $t_n$   
**Require:** Priority queue  $PQ$  of real numbers ordered from largest (highest priority) to smallest (lowest priority).

- 1: Set time to  $t_{n+1}$ , update forcing, initialize new crack set  $C_{n+1} = C_n$ .
- 2: Equilibrate elastic field, set  $PQ = \text{empty}$ .
- 3: **for** all elements  $K$  not in  $C_n$  **do**
- 4:   Compute elastic energy release  $-\Delta E_K$ .
- 5:   Compute effective crack area increment:  $\Delta A_K$ .
- 6:   Compute net energy gain:  $-\Delta F_K = -\Delta E_K - G_c \Delta A_K$ .
- 7:   If  $-\Delta F_K \geq 0$ , push  $K$  into  $PQ$ .
- 8: **end for**
- 9: **if**  $PQ \neq \text{empty}$  **then**
- 10:   Pop from  $PQ$  elements  $K$  with net energy gain  $-\Delta F_K$  within TOL of largest, add to  $C_{n+1}$ , GOTO 2.
- 11: **else**
- 12:   Exit.
- 13: **end if**

---

The next set of elements to be eroded can be determined then by keeping all elements in a priority queue according to their respective *net energy gain*, i.e., to the difference between the elastic energy released because of the erosion of the element and the corresponding fracture-energy cost, provided that the difference is positive. The queue is then popped, which supplies the next set of elements to be eroded. The criterion for popping an element is that its net energy gain is within a prescribed tolerance  $TOL$  of the maximum net energy gain among all elements. Evidently, if  $TOL = 0$ , only the element with the largest net energy gain is popped from the queue. The process is repeated till the queue is empty, i.e., until there are no elements whose erosion results in an elastic energy release greater than the corresponding fracture-energy cost. At this point, the loads are increased, and the process is repeated again. The procedure just described tends to erode elements adjacent to the current crack front, which are the most energetic, thus resulting in a continuous extension of the crack set. Three-dimensional crack growth exemplifies the need for allowing sets of elements with similar net energy gains to be popped from the queue concurrently. Thus, if erosion is restricted to take place one single element at a time, the advance of a crack in three dimensions can only occur by *zipping* along the crack front, which results in spurious transients and numerical artifacts. By contrast, if sets of elements with similar net energy gains are eroded concurrently, a three-dimensional crack can advance in lock-step along its entire front.

The key operations at the core of the crack-tracking scheme just described are the calculation of the elemental energy-release  $-\Delta E_K$  and the effective elemental area  $\Delta A_K$ . These two operations are discussed next in turn.

### 3.1. First-order estimates of elemental energy releases

We proceed to show that the elemental strain energy provides a first-order estimate of the elemental energy release, cf. [17]. This estimate is in keeping with asymptotic formulae for the energy-release rate attendant to notch-tip erosion [32].

For simplicity, we consider a linear-elastic body with stiffness matrix  $S + \Delta S_K$ , where  $\Delta S_K$  is the stiffness matrix of element  $K$  and  $S$  is the stiffness matrix of the body excluding element  $K$ . Thus, the energy released upon the erosion of the element  $K$  is

$$-\Delta E_K = \frac{1}{2}u^T(S + \Delta S_K)u - f^T u - \frac{1}{2}(u + \Delta u_K)^T S(u + \Delta u_K) + f^T(u + \Delta u_K), \quad (23)$$

where  $f$  is the applied force array,  $u$  is the displacement field prior to erosion, and  $u + \Delta u_K$  is the displacement array after erosion. Thus, by equilibrium, we have

$$(S + \Delta S_K)u = f, \quad (24a)$$

$$S(u + \Delta u_K) = f. \quad (24b)$$

By using these identities, (23) can be simplified to

$$-\Delta E_K = \frac{1}{2}u^T(\Delta S_K - \Delta S_K S^{-1} \Delta S_K)u. \quad (25)$$

Evidently, the exact evaluation of this expression requires the inversion of  $S$ , which is computationally costly. However, to first order in  $\Delta S_K$ , (25) reduces to

$$-\Delta E_K \sim \frac{1}{2}u^T \Delta S_K u, \quad (26)$$

which is explicit in the known displacements  $u$  prior to erosion and the elemental stiffness matrix  $\Delta S_K$ . Thus, explicit first-order formula (26) combines a computationally convenient estimate of the elemental energy release. This estimate is used in all subsequent calculations.

### 3.2. Implementation of contact constraint

Cracks are subject to a contact unilateral constraint upon closure. When fracture is described through eigendeformations, as in the eigenfracture scheme, the unilateral contact constraint may be enforced through constraint (22), which requires the eigendeformation  $\varepsilon^*$  to have nonnegative principal values. However, this constraint is cumbersome to implement in practice. Instead, in the calculations presented here, we resort to the simple device of restricting erosion to elements in a state of volumetric expansion, i.e., elements whose volume in the deformed configuration is larger than their undeformed volume.

### 3.3. The $\epsilon$ -neighborhood construction

Next, we concern ourselves with the practical implementation of the  $\epsilon$ -neighborhood construction required for the computation of the fracture energy. Within the eigenerosion scheme, the crack set  $C = \{\varepsilon^* \neq 0\}$  consists of the union of all eroded elements, Figure 3(a). We approximate the corresponding  $\epsilon$ -neighborhood  $C_\epsilon$  of  $C$  as the set of elements whose barycenters are at a distance less or equal to  $\epsilon$  from any of the barycenters of the eroded elements in  $C$ , Figure 3(a). The increment of crack area attendant to the erosion of a previously intact element  $K \notin C$  then follows as

$$\Delta A_K = \frac{|(C \cup K)_\epsilon \setminus C_\epsilon|}{2\epsilon}, \quad (27)$$

where  $C \cup K$  is the new crack set obtained by augmenting the old crack set  $C$  by  $K$  and  $\setminus$  denotes set difference. Thus,  $|(C \cup K)_\epsilon \setminus C_\epsilon|$  is the volume of the elements in the  $\epsilon$ -neighborhood  $(C \cup K)_\epsilon$  of the new crack set  $C \cup K$  that are not in the  $\epsilon$ -neighborhood  $C_\epsilon$  of the old crack set  $C$ , Figure 3(b).

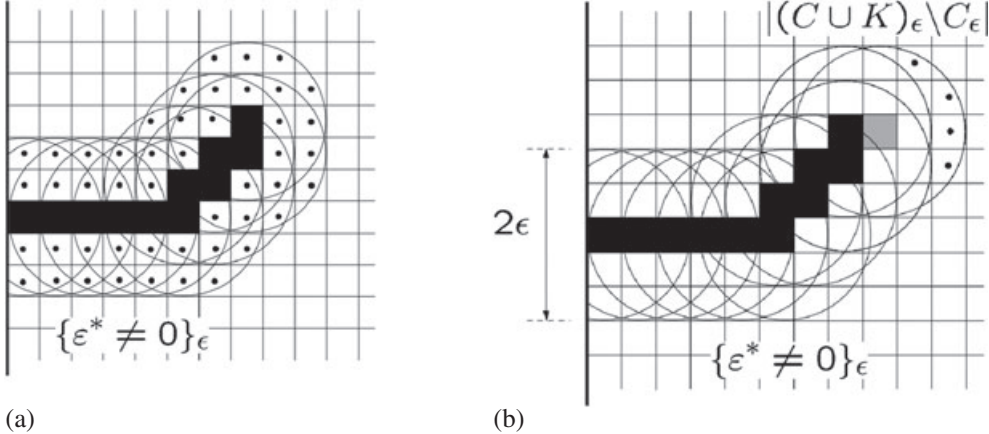


Figure 3. (a) Visualization of the crack  $\epsilon$ -neighborhood, i.e., of the set of elements belonging to the  $|K_\epsilon|$ s of eroded elements. Elements in the crack  $\epsilon$ -neighborhood are marked with black dots. (b) Visualization of the elements belonging to the incremental crack  $\epsilon$ -neighborhood,  $\Delta|K_\epsilon|$ , to be considered for the erosion test of element  $K$ . Elements in  $|K_\epsilon|$  are marked with black dots.

The size of the regularization parameter  $\epsilon$  can be chosen freely, as long as it tends to zero more slowly than the mesh size [1]. For instance, a possible choice is

$$\epsilon = C_2 \sqrt{hD}, \quad (28)$$

where  $C_2$  is a constant,  $h$  is the size of the smallest element in the mesh, and  $D$  is a characteristic size of the body. However, we have empirically found that, for purposes of convergence, it may suffice to simply take  $\epsilon$  to be proportional to  $h$ , i.e.,

$$\epsilon = C_1 h, \quad (29)$$

for some constant  $C_1$ . All the calculations presented here are based on the scheme (29) with  $C_1 = 4$ .

The implementation of the eigenerosion scheme into a standard finite-element code can be accomplished simply by keeping a list of elements belonging to the  $\epsilon$ -neighborhood  $K_\epsilon$  of each element  $K$  and by keeping a list of elements in the  $\epsilon$ -neighborhood  $C_\epsilon$  of  $C$ . As a practical matter of implementation, we additionally note that, in the case of nonuniform meshes, the size of the largest elements may exceed  $\epsilon$ . In such cases, the energy  $\Delta E_K$  released by the removal of a large element  $K$  may be in excess of the attendant fracture-energy  $G_c \Delta A_K$ , even if the elastic energy density in the element is small. To sidestep this difficulty, in calculations, we eliminate elements of size larger than  $\epsilon$  from consideration for possible erosion.

#### 4. EXAMPLES OF APPLICATION

In this section, we collect verification tests aimed at assessing the convergence characteristics of the eigenerosion scheme. We additionally present a validation example concerned with the simulation of the mixed mode I–III tests of [33]. This validation example showcases the ability of the eigenerosion scheme to simulate complex three-dimensional crack geometries.

##### 4.1. Comparison with analytical solutions

We begin by performing two-dimensional analyses on a double cantilever beam deforming in plane strain under the action of a wedging displacement  $u$  prescribed at the tip of the beams. The calculations assume linearized kinematics and employ triangular isoparametric elements with quadratic interpolation. The particular geometry of the specimen is shown in Figure 4. The beam length is  $L = 6$  and the beam half depth  $b = 0.5$ . The material is elastic, with Young modulus  $E = 1.06$  and Poisson's ratio  $\nu = 0.27$ . The critical energy-release rate is  $G_c = 0.0001$ . We consider an

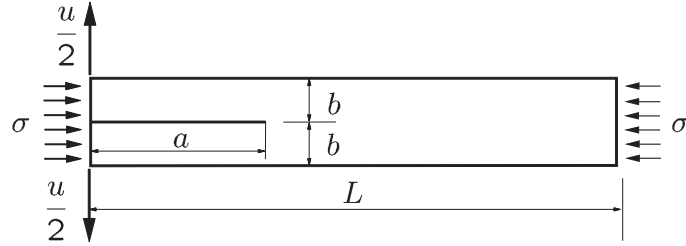


Figure 4. Geometry and displacement boundary conditions for the double cantilever beam specimen. The dimensions of the beam are  $L = 6$ ,  $b = 0.5$ , and the initial crack size is  $a = 1$ . The prescribed tip wedging displacement is  $u = 0.2$ . The material properties are  $E = 1.06$ ,  $\nu = 0.27$ , and  $G_c = 0.0001$ .

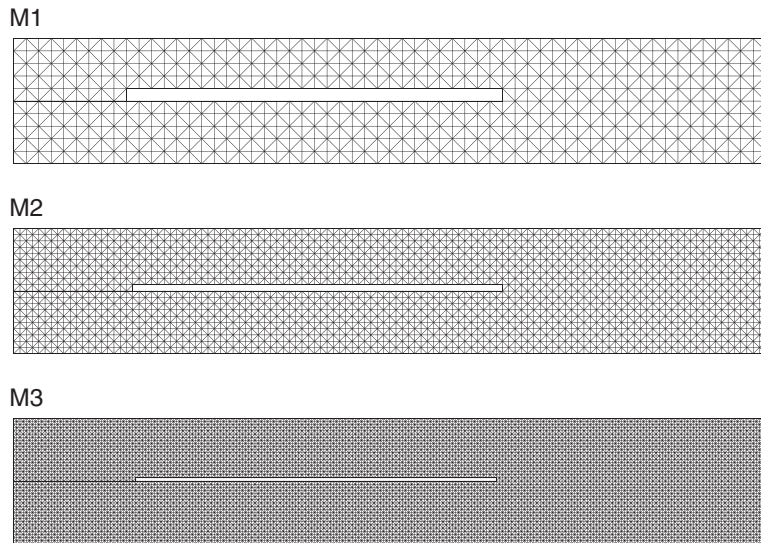


Figure 5. Final crack configuration for the three different meshes, labeled M1, M2, and M3, with mesh sizes  $h = 0.05, 0.025$ , and  $0.0125$ , respectively.

initial crack length  $a = 1$  and three uniform discretizations of mesh size  $h = 0.05, 0.025$  and  $0.0125$ , respectively. To ensure propagation within the plane of the crack, we additionally subject the specimen to a compressive  $T$ -stress  $\sigma = 0.0035$ .

Figure 5 compares the final crack configuration for the three mesh sizes. In all cases, the cracks grow within their plane through the erosion of one of the two central layers of elements. In particular, the crack thickness reduces proportionally to  $h$ . Figure 6(a) shows the computed crack length as a function of the prescribed wedging displacement. Also shown in the figure is the analytical solution obtained from linear plate theory accounting for a compressive  $T$ -force  $N$ , namely,

$$a = \frac{1}{2} \sqrt{\frac{3d^2Er^{1/2}u}{3d^2E + Nr^{1/2}(1 - \nu^2)}}, \quad (30)$$

where we write

$$r = \frac{3E}{G_c(1 - \nu^2)} d^3 \quad (31)$$

(see Appendix A for the derivation). As may be seen from figure, the numerical solutions compare well with the analytical solution and are ostensibly converged with respect to mesh size. The small discrepancy between the analytical and numerical solutions mainly reflects the limited accuracy of plate theory applied to the geometry of the specimen. We also note that the initial lag in crack

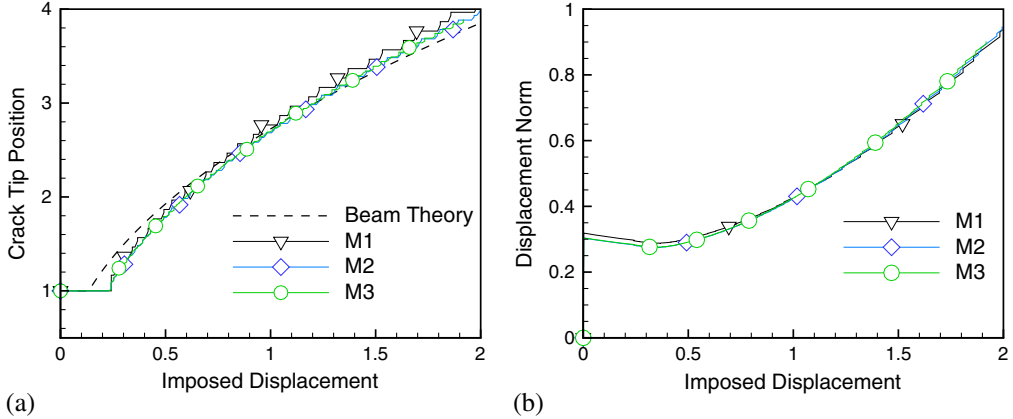


Figure 6. Convergence analysis for crack propagation in a compressed double cantilever beam loaded in plane strain. (a) Crack-tip evolution with the imposed displacement: comparison between the beam theory solution Equation (30) and the numerical results for three mesh sizes M1, M2, and M3. (b)  $L^1$ -displacement norm as a function of the prescribed tip wedging displacement.

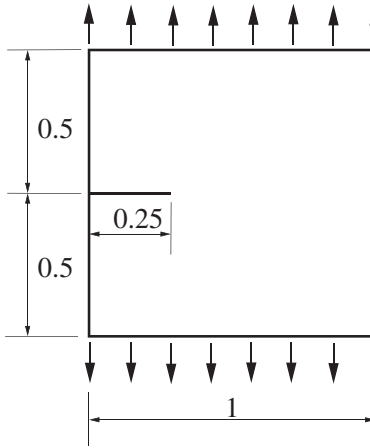


Figure 7. Edge-crack plate test. Geometry and displacement boundary conditions.

growth is due to an underestimation of the effective crack advance by the  $\epsilon$ -neighborhood construction during the erosion of the first element at crack initiation. We additionally recall from [1] that the eigenerosion displacements converge strongly in the  $L^1$ -norm. The dependence of the  $L^1$ -norm of the displacement field on the prescribed wedging displacement is shown in Figure 6(b) for the three mesh sizes under consideration. We observe from the figure that the  $L^1$ -norm of the displacement field is ostensibly converged with respect to mesh size, consistently with  $L^1$ -convergence of the displacement field.

#### 4.2. Edge-cracked square panel in mode I

Next, we assess the performance of the eigenerosion scheme in two-dimensional and three-dimensional tests concerned with plane-strain crack growth in mode I. We specifically consider a square plate of size  $H = 1$  containing an initial edge crack of length  $a = 0.25H$  loaded in pure mode I by displacement control on the outer flanks of the plate, Figure 7. The two-dimensional calculations are performed for a linear-elastic Hookean material, whereas the three-dimensional calculations are carried out in finite deformations for a compressible neo-Hookean material. In both cases, the Young's modulus is  $E = 1.06$ , the Poisson's ratio  $\nu = 0.333$ , and critical energy-release rate  $G_c = 0.0001$ . Four structured meshes with element sizes  $1/40 H$ ,  $1/80 H$ ,  $1/160 H$ , and

$1/320 H$  are considered, Figure 8. The edge-cracked panel loaded in mode I provides an illustration of how the variational formulation of fracture, namely, the minimization of energy-dissipation functional (21) subject to irreversibility and contact constraints (10) and (11), respectively, and the implementation of the eigenerosion scheme listed in (1) handle situations of unstable crack growth characterized by *finite jumps* of the crack front. Thus, Figure 9 depicts the dependence of the strain energy  $E$  of the body on crack extension  $\Delta a$  at fixed prescribed boundary displacement  $\delta$ . As it may be seen from the figure, the strain energy is a *decreasing and concave* function of crack length. Let  $E_0(\delta)$  be the elastic energy in the panel at prescribed boundary displacement  $\delta$  and zero crack extension,  $\Delta a = 0$ . Evidently, the elastic energy released when the entire initial ligament is cracked is  $E_0(\delta)$ . In addition, the corresponding expenditure of fracture energy is  $G_c l$ , where  $l = 0.75$  is the initial ligament length. If we restrict crack growth to the plane of the crack, because of the concavity of the elastic energy with respect to crack advance, it follows that the initial crack is stable for as long as  $E_0(\delta) < G_c l$ , i.e., any crack extension  $\Delta a$  requires a fracture-energy expenditure in excess of the elastic energy released. Thus, energy-dissipation functional (21) is minimized for zero crack extension,  $\Delta a = 0$ . Let  $\delta_c$  be the critical prescribed boundary displacement at which  $E_0(\delta_c) = G_c l$ .

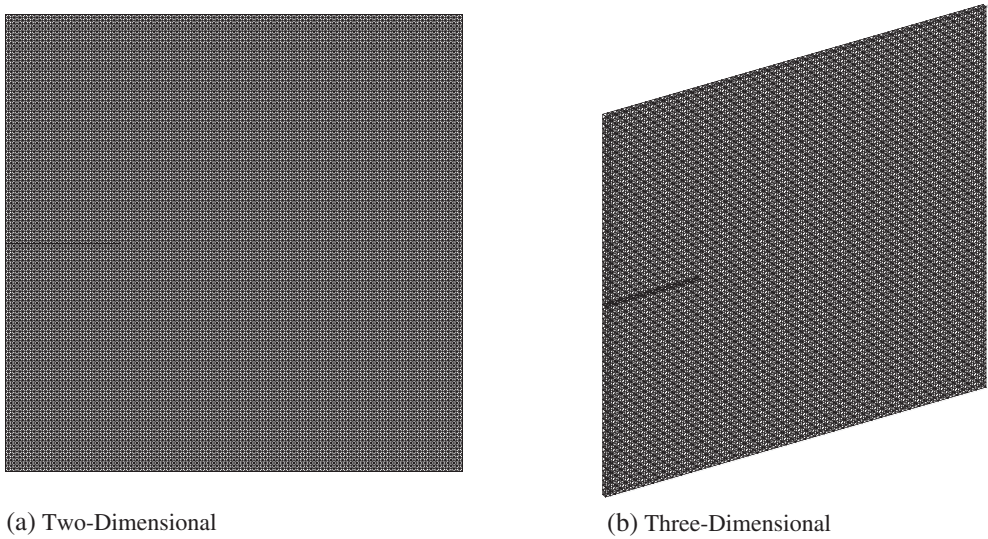


Figure 8. Edge-crack plate test. Finest structured meshes used in calculations. (a) Two-dimensional mesh.  
(b) Three-dimensional mesh.

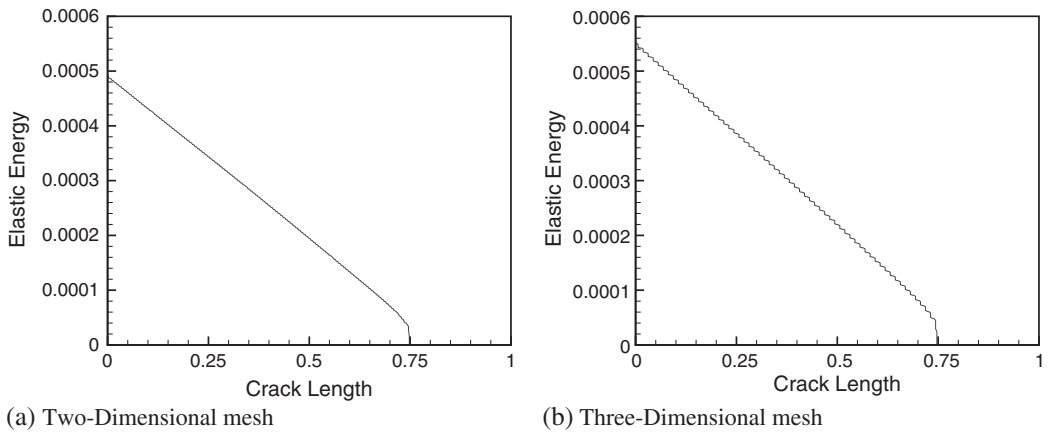


Figure 9. Edge-cracked square panel. Dependence of the strain energy on crack length at fixed prescribed boundary displacement. (a) Two-dimensional mesh. (b) Three-dimensional mesh.

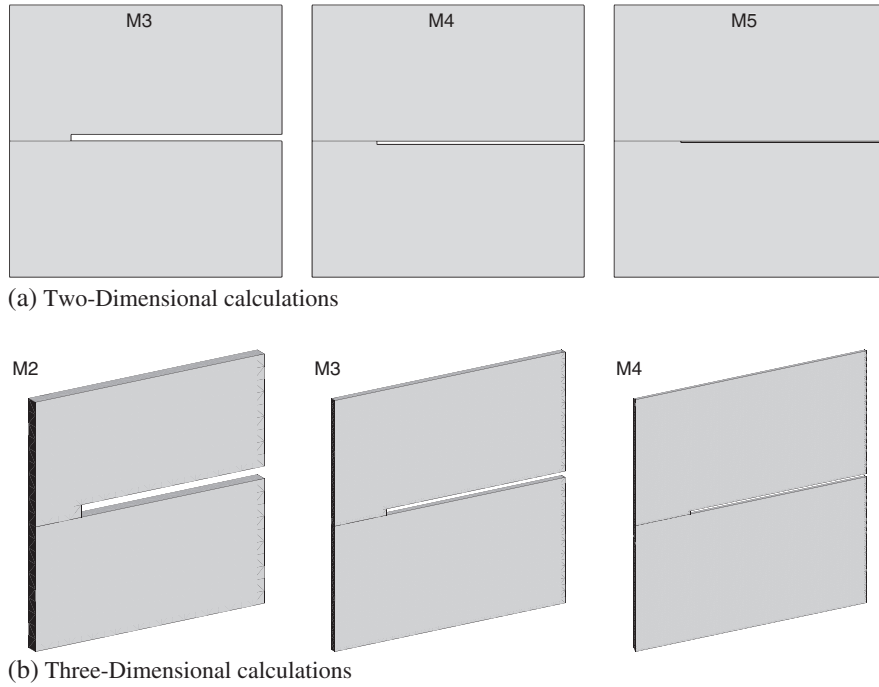


Figure 10. Edge-cracked square panel. Computed final crack geometries. (a) Two-dimensional calculations.  
(b) Three-dimensional calculations.

Then, for any  $\delta > \delta_c$ , there is an exchange of stability, and energy-dissipation functional (21) is minimized for  $\Delta a = l$ , i.e., by extending the crack through the entire initial ligament. We may interpret this exchange of stability as resulting in a *discrete jump* of the crack of length  $\Delta a = l$ . We also note that intermediate crack extensions  $0 < \Delta a < l$  are not energy-dissipation minimizers for any prescribed boundary displacement  $\delta$  and, therefore, are devoid of special meaning within the variational framework. This lack of continuous crack-tracking capability through discrete jumps has been sometime regarded as a shortcoming of the theory and has provided impetus for several extensions thereof, see for example [34].

Figure 10 shows the final crack geometry for three mesh sizes and for two-dimensional and three-dimensional analyses computed from algorithm (1). As may be seen from the figure, the crack grows within its plane through the erosion of one row of elements, and the thickness of the crack reduces proportionally to  $h$ . As noted in the foregoing, within the present variational framework, the final crack configuration is the result of a discrete jump from the initial crack configuration across the entire initial ligament, whereupon the panel completely unloads. Indeed, the computed global reaction  $E'(\delta)$  drops to zero upon the attainment of the critical prescribed boundary displacement  $\delta_c$  for exchange of stability, Figure 11. We also observe from the figure that the numerical solutions are ostensibly converged with respect to mesh size.

Also within the strict confines of the present variational framework, the final configuration of the crack follows from the *global minimization* of energy-dissipation functional (21) with respect to all crack sets containing the initial precrack. However, global optimization is notoriously complex and computationally costly. Instead, as a matter of computational expediency algorithm, crack-tracking scheme (1) updates the crack set through a sequence of ‘flips’, with each flip corresponding to the erosion of a small number of selected elements. This continuation strategies based on flips between neighboring configurations are characteristic of Monte Carlo and other global optimization schemes. Although computationally efficient, continuation schemes do not identify global minimizers in general. However, as already noted, it may be contrariwise argued that the resulting constrained theory is more physically meaningful than strict global minimization of the energy-dissipation

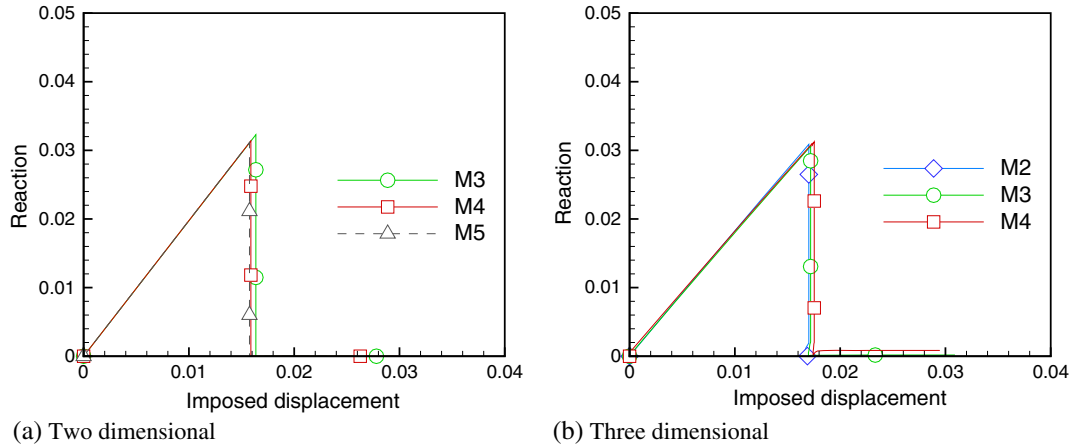


Figure 11. Edge-cracked square panel. Dependence of global reaction force on prescribed boundary displacement. (a) Two-dimensional calculations. (b) Three-dimensional calculations.

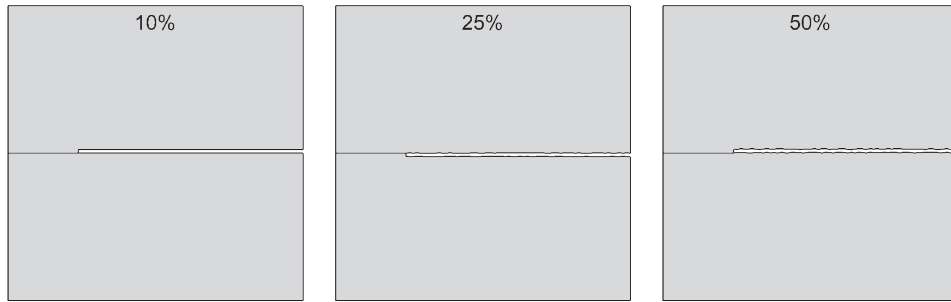


Figure 12. Mode I case. Crack paths for random two-dimensional meshes of size  $h = 1/320 H$ . The mesh is randomized by giving the nodes random displacements with uniform probability within the intervals  $0.1 h$ ,  $0.25 h$ , and  $0.50 h$ , respectively.

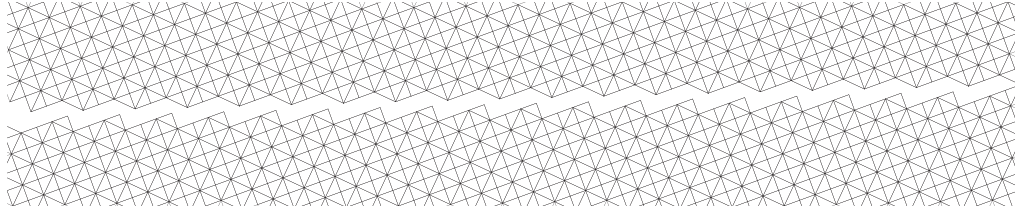


Figure 13. Mode I case. Detail of the crack paths for a uniformly biased two-dimensional mesh wherein the elements are aligned  $20^\circ$  with respect to the precrack plane. Mesh size  $h = 1/160 H$ .

functional (21). Other solution strategies for calculations based on the Ambrosio–Tortorelli functional have been developed and carefully assessed by Bourdin [29–31].

We recall that the main intent of the  $\epsilon$ -neighborhood construction is to eliminate the mesh bias that afflicts naive erosion schemes. We test the effectiveness of the  $\epsilon$ -neighborhood construction in that regard by repeating the mode I edge-cracked panel calculations for random meshes. Specifically, we randomize the meshes shown in Figure 8 by giving the nodes random displacements with uniform probability within the intervals  $0.1h$ ,  $0.25h$ , and  $0.50h$ , with  $h = 1/320 H$ . Figure 12 shows the resulting final crack configurations. As may be observed from the figure, the computed crack path is insensitive to the randomness of the mesh. A perhaps even more exacting test of the ability of the  $\epsilon$ -neighborhood construction to compensate for mesh bias concerns meshes that are systematically slanted with respect to the direction of propagation of the crack. Figures 13 and 14 present

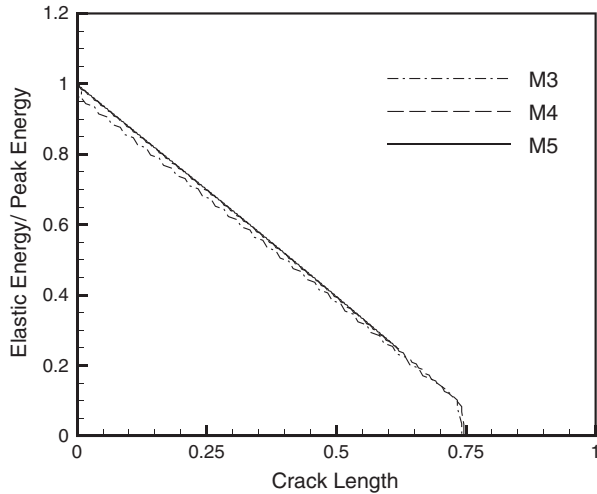


Figure 14. Mode I case. Elastic strain energy versus crack length for  $20^\circ$  uniformly biased meshes of sizes  $h = 1/80 H$ ,  $h = 1/160 H$ , and  $h = 1/360 H$ .

one such test consisting of an edge-cracked panel subjected to mode I loading in which the mesh is slanted throughout at an angle of  $20^\circ$  to the direction of crack propagation. As may be seen from Figure 13, the crack zigzags around the exact propagation path and converges to it as the mesh is refined. Moreover, owing to the  $\epsilon$ -neighborhood construction, the fracture-energy cost attendant to crack propagation is proportional to the *projected* or nominal area of the crack. In particular, the zigzagging of the crack does not result in an overestimation of the fracture energy, which is mesh-insensitive and converges to the exact value in the limit of vanishing mesh size.

#### 4.3. Mixed mode I–III crack growth in three-point bending configuration

Our final example assesses the ability of the eigenerosion scheme to track crack growth in three dimensions. We specifically aim to simulate the mixed mode I–III experiments of [33] on PMMA prenotched plates loaded in a three-point-bending configuration. In homogeneous and ostensibly linear-elastic isotropic materials, a growing crack in a plate of finite width loaded in mixed I–III mode is often observed to turn toward a pure Mode I orientation [33, 35–37]. The rotation of the crack front can be either abrupt or gradual, and it can happen in uniformly or in a *factory-roof* pattern, depending on the loading conditions, the material, and the width of the plate. A linearized stability analysis of mixed mode I–III crack growth in an infinite linear-elastic isotropic solid was performed by [38]. The analysis reveals the existence of a critical ratio of mode III to mode I stress-intensity factor at which an exchange of stability takes place between planar crack growth and growth in factory-roof pattern. Full numerical calculations of mixed mode I–III crack growth also presented by [38] show that the factory-roof pattern undergoes period doubling, which in turn results in the progressive coarsening of the pattern with increasing crack advance. In plates of finite width, it is possible—and indeed experimentally observed—for a crack to turn uniformly over its entire front, although the factory-roof mode may be expected to dominate in the interior of the plate in the early stages of crack growth at crack-advance lengths much smaller than the plate width.

In keeping with the experiments of [33], we consider plates 260 mm long, 60 mm deep, and 10 mm thick precracked at  $15^\circ$ ,  $30^\circ$ , and  $45^\circ$  to the front face, Figure 15(a). The inclination of the precrack results in an initial mixed mode I–III loading of the crack front. We restrict calculations to the central section of the specimen of thickness  $b = 30$  mm, Figure 15(b), and apply the equivalent static boundary conditions representative of three-point bending, Figure 15(b). The load  $P$  is monotonically increased until the crack traverses the entire specimen. Also in keeping with [33], we assume a Young's modulus  $E = 2800$  MPa, a Poisson's ratio  $\nu = 0.38$ , and critical energy-release rate  $G_c = 0.352$  N/mm (cf. [39]). In calculations, we model the material as compressible

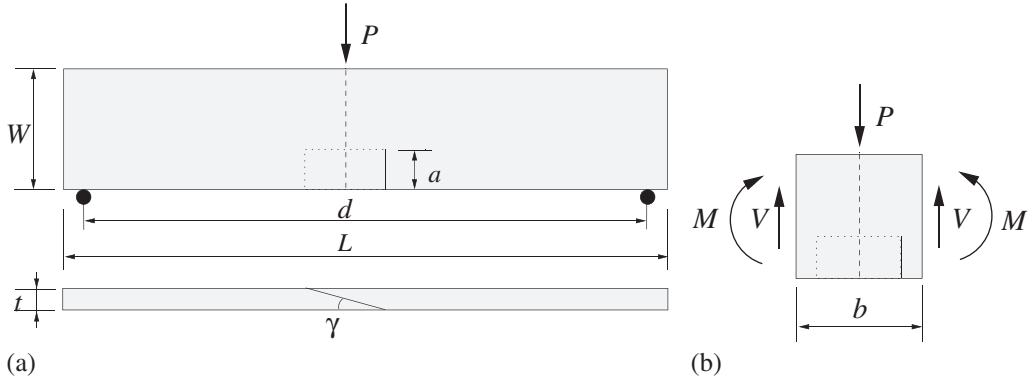


Figure 15. Mixed mode I–III crack growth in three-point bending configuration. (a) Poly-methyl methacrylate specimen loaded in a three-point bending configuration [33]. The distance between the supports is  $d = 240$  mm, the specimen length is  $L = 260$  mm, the depth is  $W = 60$  mm, and the thickness is  $t = 10$  mm. The notch length is  $a = 20$  mm and the notch inclination  $\gamma = 15^\circ, 30^\circ, 45^\circ$ . (b) In the present numerical simulations, only the central  $b = 30$  mm are modeled, and the corresponding static boundary conditions are enforced, i.e.,  $V = P/2$  and  $M = P(d - b)/4$ .

neo-Hookean and account for finite kinematics. The three meshes used in the simulations are displayed in Figure 16. The element size of all meshes is  $h = 1$  mm. The meshes contain in the order of 120,000 nodes and 80,000 10-node tetrahedral elements.

Figure 17 gives snapshots of the computed crack geometries after extensive growth. The rendering of the crack surface is suggested by the  $\epsilon$ -neighborhood construction and merits special remark. Thus, in the eigenerosion scheme, the crack set consists of a collection of eroded elements and therefore, is rough and of a thickness commensurate with the mesh size. However, we may regard the  $\epsilon$ -neighborhood construction as defining a smoothed out *effective crack surface*, namely, the surface whose  $\epsilon$ -neighborhood coincides with the  $\epsilon$ -neighborhood of the element-wise crack set. In rendering the crack set, we approximate the effective crack surface by means of spline functions and a smoothing algorithm. In all figures, we additionally mark the barycenters of the eroded elements to display the unprocessed results.

As already noted, both analytical studies [38] and experimental observations [33] reveal that the initial notch growths through the development of a microscopic factory-roof profile. For a plate of finite thickness, the crack subsequently turns in its entirety to attain a mode I configuration [33]. Whereas the initial microscopic factory-roof profile cannot be resolved by the present meshes, it is evident from Figure 17 that the overall turning of the crack is well captured by the eigenerosion scheme.

A quantitative comparison between simulations and experiment can be based on the initial kink angles  $\alpha_R$  and  $\alpha_L$  on the right and left specimen surface, respectively. Table I compiles the experimentally measured average kink angles, obtained by averaging the kink angles on both surfaces of the specimen, and the corresponding numerical values. As may be seen from this comparison, the eigenerosion calculations capture the general trend of increasing kink angle with increasing precrack inclination and mode III component and results in modest numerical errors.

## 5. SUMMARY AND CONCLUDING REMARKS

The preceding work is concerned with the implementation, verification, and validation of a variant of the eigenfracture scheme of [1] based on element erosion, which we have referred to as *eigenerosion*. In the eigenfracture scheme, the energy functional depends on two fields: the displacement field and an eigendeformation field that describes such cracks as may be present in the body. Specifically, eigendeformations allow the displacement field to develop jumps at no cost in local elastic energy. In addition, in the eigenfracture scheme, the fracture energy is set to be proportional to the volume of the  $\epsilon$ -neighborhood of the support of the eigendeformation field, suitably scaled by  $1/\epsilon$ . The

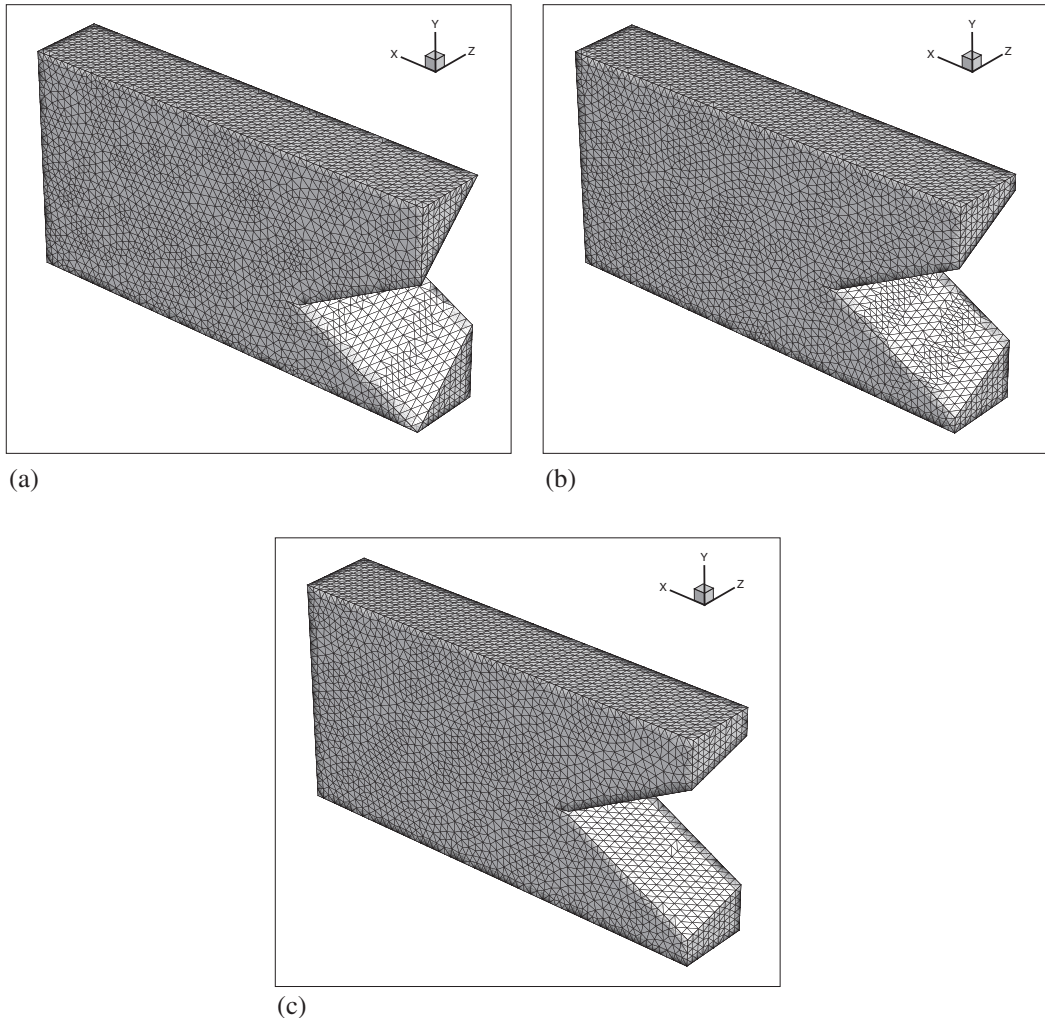


Figure 16. Mixed mode I-III crack growth in three-point bending configuration. Meshes used in calculations. Notch is enlarged by removing the essentially unstressed region adjacent to its flanks to facilitate the visualization of the crack front. (a) Initial inclination angle  $\gamma = 45^\circ$ . The mesh consists of 120,814 nodes and 83,143 10-noded tetrahedral elements. (b) Initial inclination angle  $\gamma = 60^\circ$ . The mesh consists of 115,840 nodes and 79,500 10-noded tetrahedral elements. (c) Initial inclination angle  $\gamma = 75^\circ$ . The mesh consists of 115,049 nodes and 79,128 10-noded tetrahedral elements.

optimal crack set is obtained by minimizing the resulting energy functional with respect to both the displacement and the eigendeformation fields, subject to irreversibility constraints. The eigenerosion scheme is derived from the general eigenfracture formulation by restricting the eigendeformations in a binary sense: they can be either zero, in which case the local behavior is elastic, or they can be equal to the local displacement gradient, in which case the corresponding material neighborhood is failed, or *eroded*. When combined with a finite-element approximation, this scheme gives rise to *element erosion*, i.e., the elements can be either intact, in which case their behavior is elastic, or be completely failed, or eroded, and have no load bearing capacity. However, in contrast to other erosion schemes that fail to converge or converge to the wrong limit [21], the eigenfracture scheme is known to properly converge to Griffith fracture in the limit of vanishingly small mesh sizes [1]. In particular, the local-neighborhood averaging of the energy that underlies the calculation of the effective energy release has the effect of eliminating spurious mesh-dependencies. The implementation of the method, included the all-important  $\epsilon$ -neighborhood construction, is exceedingly simple and applies to general situations, possibly involving complex three-dimensional fracture patterns such

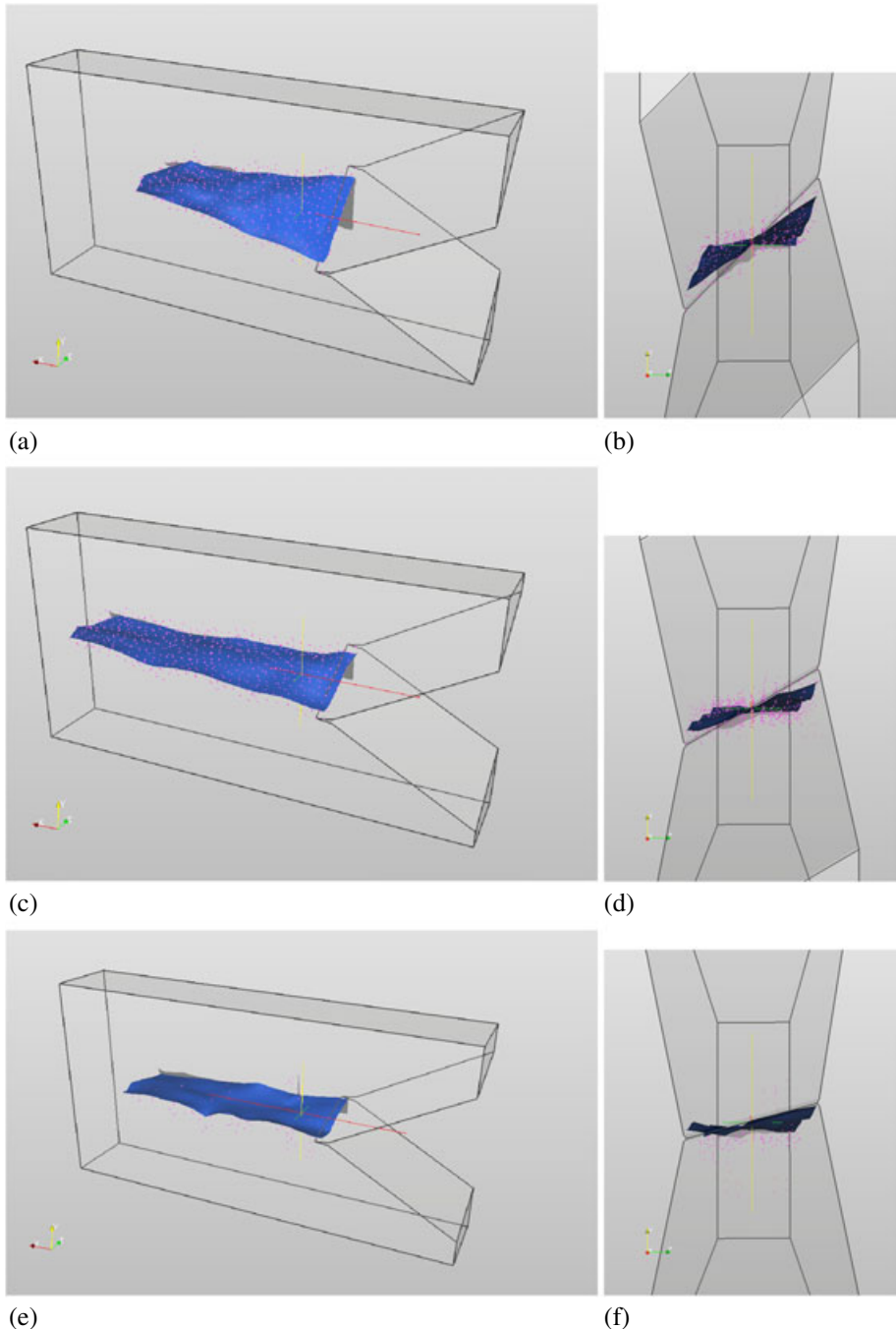


Figure 17. Mixed mode I–III crack growth in three-point bending configuration. Crack surfaces computed from the eigenerosion scheme. (a) Initial inclination angle  $\gamma = 45^\circ$ , top view. (b) Initial inclination angle  $\gamma = 45^\circ$ , front view. (c) Initial inclination angle  $\gamma = 60^\circ$ , top view. (d) Initial inclination angle  $\gamma = 60^\circ$ , front view. (e) Initial inclination angle  $\gamma = 75^\circ$ , top view. (f) Initial inclination angle  $\gamma = 75^\circ$ , front view.

as branching and fragmentation. The accuracy and fidelity of the eigenerosion approach have been assessed through convergence studies for mode I crack growth, both in two and three dimensions and for structured and random meshes, and validated against experiments concerned with mixed mode I–III fracture of PMMA plates ([33]).

Table I. Mixed mode I–III crack growth in three-point bending configuration.  
Experimental [33] and numerical initial kink angles.

$\gamma$	$\alpha$ [33]	$\alpha_R$	$\alpha_L$	$\alpha$	error %
75	21.1	22	18	20.0	5.1
60	38.4	36	35	35.5	7.6
45	61.9	57	58	57.5	7.1

$\alpha$  denotes the average kink angle,  $\alpha_R$  the kink angle on the right surface, and  $\alpha_L$  the kink angle on the left surface. All angles are reported in degrees.

Overall, the present eigenerosion scheme performs in the manner typical of low-order methods: it is robust with respect to mesh convergence, versatile and convenient as regards applicability, and exhibits fair accuracy and fidelity. One advantage of the eigenerosion scheme is that it can be readily built on top conventional finite element and material models and does not require element enrichment or the resolution of the boundary layers typical of regularized models. The coarseness of the crack set obtained by element erosion can be palliated during postprocessing by means of surface reconstruction techniques. This postprocessing is fair and germane to the method as it simply reconstructs the effective crack surface that is implied by the  $\epsilon$ -neighborhood construction.

Finally, we remark that the variational approach to fracture, on which we have constructed the method and by which fracture is recast as a free-discontinuity problem, is fraught with well-known difficulties. In particular, reliance on global minimization to define the crack set may lead to nonphysical or pathological results. We therefore emphasize that many of the elements of the eigenerosion scheme, including the use of eigendeformations to define the crack set and the  $\epsilon$ -neighborhood construction that assigns to it a mesh-independent fracture energy, are independent of the variational framework. Indeed, the continuation algorithm used in the present study to track crack growth signifies a departure from the strict variational framework. An additional nonvariational framework for the application of the eigenerosion scheme is explicit dynamics in, for example, as regards ballistic penetration applications [40–42].

## APPENDIX A

We consider the double cantilever beam in Figure 4. When a wedging displacement  $u$  is applied to the two arms, the reaction  $P$  is

$$P = \frac{1}{8} \frac{E' d^3}{a^3} u,$$

where  $E' = E/(1 - \nu^2)$  (plane strain), leading to a bending moment  $M$  at the crack tip

$$M = Pa = \frac{1}{8} \frac{E' d^3}{a^2} u.$$

The linear beam theory provides the analytical expression of the energy-release rate  $G$  for a purely bent double cantilever beam in plane-strain condition [43]:

$$G = \frac{3}{16} E' \frac{b^3}{a^4} u^2.$$

For  $G = G_c$ , the aforementioned relation furnishes

$$a = \frac{1}{2} r^{1/4} u^{1/2}, \quad (32)$$

with  $r$  defined in (31). In the presence of an axial force  $N$ , the maximum positive stress in the beam is

$$\sigma = \frac{N}{d} + \frac{3E'd}{4a^2} u.$$

The same stress is reached in pure bending for a different displacement  $\bar{u}$ , such that

$$\sigma = \frac{3E'd}{4a^2}\bar{u}.$$

Thus, we can write

$$u = \bar{u} - \frac{4}{3} \frac{N}{E'} \frac{a^2}{d^2}.$$

The crack-tip advance  $a$  in the presence of a compressive force follows as the solution of (32) written in the form

$$a^2 = \frac{1}{4}r \left( \bar{u} - \frac{4}{3} \frac{N}{E'} \frac{a^2}{d^2} \right).$$

#### ACKNOWLEDGEMENTS

The collaboration of Santiago Lombeyda for the rendering of the crack pictures is gratefully acknowledged. AP wants to thank Michael Aivazis for his clear and helpful introduction to parallel computing. This material is based upon work supported by the Department of Energy National Nuclear Security Administration under Award Number DE-FC52-08NA28613 through Caltech's ASC/PSAAP Center for the Predictive Modeling and Simulation of High-Energy Density Dynamic Response of Materials.

#### REFERENCES

1. Schmidt B, Fraternali F, Ortiz M. Eigenfracture: an eigendeformation approach to variational fracture. *SIAM Multiscale Modeling and Simulation* 2009; **7**:1237–1266.
2. Ambrosio L, Tortorelli VM. On the approximation of free discontinuity problems. *Bollettino dell'Unione Matematica Italiana* 1992; **B 7**:105–123.
3. Braides A, Dal Maso G. Nonlocal approximation of the mumford-shah functional. *Calculus of Variations and Partial Differential Equations* 1997; **5**:293–322.
4. Braides A, Defranceschi A. *Homogenization of Multiple Integrals*. Clarendon Press: Oxford, 1998.
5. Francfort GA, Marigo J-J. Revisiting brittle fracture as an energy minimization problem. *Journal of the Mechanics and Physics of Solids* 1998; **46**(8):1319–1342.
6. Chambolle A. A density result in two-dimensional linearized elasticity and applications. *Archive of Rational Mechanics and Analysis* 2001; **111**:211–233.
7. Francfort GA, Larsen CJ. Existence and convergence for quasi-static evolution in brittle fracture. *Communications on Pure and Applied Mathematics* 2003; **56**:1465–1500.
8. Dal Maso G, Francfort GA, Toader R. Quasistatic crack growth in nonlinear elasticity. *Archive of Rational Mechanics and Analysis* 2005; **176**(2):165–225.
9. Dal Maso G, Toader R. A model for the quasi-static growth of brittle fractures: existence and approximation results. *Archive of Rational Mechanics and Analysis* 2002; **162**(2):101–135.
10. Braides A.  $\Gamma$ -convergence for Beginners. Oxford University Press: Oxford UK, 2002.
11. De Giorgi E, Ambrosio L. Un nuovo funzionale del calcolo delle variazioni. *Accademia Nazionale dei Lincei - Rendiconti della Classe di Scienze Fisiche, Matematiche e Naturali* 1988; **82**:199–210.
12. Dal Maso G. An Introduction to  $\Gamma$ -convergence. Birkhäuser: Boston MA USA, 1993.
13. Ambrosio L, Fusco N, Pallara D. *Functions of Bounded Variation and Free Discontinuity Problems*. Oxford University Press: Oxford, 2000.
14. Mura T. *Mechanics of Defects in Solids*. Martinus Nijhoff: Dordrecht, 1987.
15. Johnson GR, Stryk RA. Eroding interface and improved tetrahedral element algorithms for high velocity impacts in three dimensions. *International Journal of Impact Engineering* 1987; **5**:414–427.
16. Belytschko T, Lin J. A three-dimensional impact-penetration algorithm with erosion. *International Journal of Impact Engineering* 1988; **5**(1–4):111–127.
17. Ortiz M, Giannakopoulos AE. Crack propagation in monolithic ceramics under mixed mode loading. *International Journal of Fracture* 1990; **44**:233–258.
18. Johnson GR, Stryk RA. User instruction for the 1990 version of the combined (1d,2d,3d) epic code. *Technical Report DE-AC04-87AL-42550*, DARPA, 1990.
19. Whirley RG, Hallquist JO. Dyna-3d user manual. *Technical Report UCRL-MA-107254*, Lawrence Livermore National Laboratory, 1991.
20. Borvik T, Hopperstad OS, Pedersen KO. Quasi-brittle fracture during structural impact of aa7075-t651 aluminum plates. *International Journal of Impact Engineering* 2008; **37**:537–551.

21. Negri M. Finite element approximation of the Griffith's model in fracture mechanics. *Numerische Mathematik* 2003; **95**(4):653–687.
22. Larsen CJ, Ortiz M, Richardson CL. Fracture paths from front kinetics: relaxation and rate-independence. *Archive of Rational Mechanics and Analysis* 2009; **193**:539–583.
23. Knees D, Mielke A. Energy release rate for cracks in finite-strain elasticity. *Advances in Mathematical Sciences and Applications* 2008; **31**:501–528.
24. Coleman BD, Noll W. The thermodynamics of elastic materials with heat conduction and viscosity. *Archive of Rational Mechanics and Analysis* 1963; **13**:167–179.
25. Negri M. A discontinuous finite element approximation of free discontinuity problems. *Advances in Mathematical Sciences and Applications* 2005a; **15**:283–306.
26. Negri M. A non-local approximation of free discontinuity problems in *SBV* and *SBD*. *Calculus of Variations and Partial Differential Equations* 2005b; **25**:33–62.
27. Lussardi L, Negri M. Convergence of non-local finite element energies for fracture mechanics. *Numerical Functional Analysis and Optimization* 2007; **28**:83–109.
28. Ortiz M. A constitutive theory for the inelastic behavior of concrete. *Mechanics of Materials* 1985; **4**:67–93.
29. Bourdin B, Chambolle A. Implementation of an adaptive finite element approximation of the Mumford–Shah functional. *Numerische Mathematik* 2000; **85**:608–646.
30. Bourdin B, Francfort GA, Marigo JJ. Numerical experiments in revisited brittle fracture. *Journal of the Mechanics and Physics of Solids* 2000; **48**:797–826.
31. Bourdin B. Numerical implementation of the variational formulation of brittle fracture. *Interface Free Bound* 2007; **9**:411–430.
32. Rice JR. *Mathematical Analysis in the Mechanics of Fracture*. Academic Press: New York, 1968.
33. Lazarus V, Buchholz F-G, Fulland M, Wiebesiek J. Comparison of prediction by mode II or mode III criteria on crack front twisting in three or four point bending experiments. *International Journal of Fracture* 2008; **153**:141–151.
34. Larsen CJ. Epsilon-stable quasi-static brittle fracture evolution. *Communications on Pure and Applied Mathematics* 2010; **63**:630–654.
35. Lazarus V, Leblond JB. Crack paths under mixed mode (I + III) or (I + II + III) loadings. *Comptes Rendus de l'Académie des Sciences, Série II (Mécanique, Physique, Astronomie)* 1998; **326**:171–177.
36. Lazarus V, Leblond JB, Mouchrif SE. Crack front rotation and segmentation in mixed mode I + III or I + II + III. Part II: comparison with experiments. *Journal of the Mechanics and Physics of Solids* 2002; **49**:1421–1443.
37. Buchholz FG, Chergui A, Richard HA. Fracture analysis and experimental results of crack growth under general mixed mode loading conditions. *Engineering Fracture Mechanics* 2004; **71**(4–6):455–468.
38. Xu G, Bower AF, Ortiz M. An analysis of non-planar crack growth under mixed mode loading. *International Journal of Solids and Structures* 1994; **31**:2167–2193.
39. Yu RC, Pandolfi A, Ortiz M. A 3D cohesive investigation on branching for brittle materials. In *IUTAM Symposium on Discretisation Methods for Evolving Discontinuities*, Combescure A, de Borst R, Belytschko T (eds). IUTAM Bookseries: Lyon, France, 2007; 139–151.
40. Li B, Kidane A, Ravichandran G, Ortiz M. Optimal transportation meshfree simulation of terminal ballistics. *International Journal of Impact Engineering* 2012; **42**:25–36.
41. Kidane A, Lashgari A, Li B, McKerns M, Ortiz M, Owhadi H, Ravichandran G, Stalzer M, Sullivan TJ. Rigorous model-based uncertainty quantification with application to terminal ballistics—part I: systems with controllable inputs and small scatter. *Journal of the Mechanics and Physics of Solids* 2012; **60**:983–1001.
42. Adams M, Lashgari A, Li B, McKerns M, Mihaly J, Ortiz M, Owhadi H, Rosakis AJ, Stalzer M, Sullivan TJ. Rigorous model-based uncertainty quantification with application to terminal ballistics—part II. Systems with uncontrollable inputs and large scatter. *Journal of the Mechanics and Physics of Solids* 2012; **60**:1002–1019.
43. Hutchinson JW. A course in nonlinear fracture mechanics, Technical University of Denmark, Lyngby, 1979.